energies

MDPI

Article

Reconstruction and Prediction of Three-Dimensional Transient Flow Field in a Draft Tube of Francis Turbine Using Sparse Sensors and a Proper Orthogonal Decomposition-Long Short-Term Memory Network

Lisheng Zhang [1,2], Ming Ma [1,3], Yongbo Li [1,3], Lijun Kong [1,3], Lintao Xu [1,3], Zhenghai Huang [1,3] and Bofu Wang [1,4,*]

[1] Hubei Technology Innovation Center for Smart Hydropower, Wuhan 430014, China
[2] College of Hydraulic and Environmental Engineering, China Three Gorges University, Yichang 443002, China
[3] China Yangtze Power Co., Ltd., Beijing 100032, China
[4] School of Mechanics and Engineering Science, Shanghai University, Shanghai 200444, China
* Correspondence: bofuwang@shu.edu.cn

Abstract

The accurate reconstruction and real-time prediction of transient three-dimensional flow fields in hydraulic turbines are critical for ensuring operational stability under renewable energy-driven variable-load conditions, yet conventional computational fluid dynamics (CFD) approaches remain too computationally expensive for digital twin applications. This paper proposes a hybrid framework that integrates Proper Orthogonal Decomposition (POD) with Long Short-Term Memory (LSTM) networks to reconstruct and predict the unsteady flow field within the draft tube of a Francis turbine using only four sparse wall-mounted pressure sensors. The methodology begins with high-fidelity Large Eddy Simulation (LES) to establish a comprehensive flow field database under Part Load (PL), Best Efficiency Point (BEP), and High Load (HL) conditions. POD is subsequently applied to extract dominant coherent structures and their temporal coefficients, achieving a low-dimensional representation of the high-dimensional flow field. A comparative analysis between standard POD and weighted POD reveals that under the PL condition characterized by a strong double-helical vortex rope, the weighting effect is significant—standard POD captures 90% of the total energy with the first 2 modes, while weighted POD requires up to 8 modes to reach the same threshold. Under the BEP and HL conditions, the energy distributions of the two methods are nearly identical, yet weighted POD still yields cleaner spatial modes with sharper vortex boundaries and fewer spurious wall-region vortices. An LSTM network is then trained to establish a mapping between time-series signals from the four sensors and the POD temporal coefficients. The results demonstrate that LSTM prediction performance is governed by the spatial correlation between each mode and the sensor locations rather than by temporal regularity. Modes that project strongly onto the sensor locations—PL Modes 1–2 (R^2 = 0.85 and 0.513), BEP Mode 1 (R^2 = 0.96), and HL Mode 1 (R^2 = 0.92)—are reliably predictable, while PL Mode 3 and HL Mode 2, despite their regular temporal oscillations, yield strongly negative R^2 values (−3.366 and −186.6) because their spatial structures are concentrated away from the wall. With a condition-adaptive strategy predicting only sensor-correlated, energetic modes, the reconstructed pressure fields achieve mean L2 relative errors of 17.01% (PL), 7.17% (BEP), and 12.91% (HL). Because the mean flow dominates total pressure energy (86.66–98.07%), the effective absolute error is substantially lower. The proposed POD-LSTM framework successfully bridges the gap between high-fidelity CFD and real-time monitoring, enabling full-field flow state estimation from sparse sensor measurements without the computational expense

Check for updates

Academic Editor: Helena M. Ramos

Received: 30 March 2026
Revised: 30 April 2026
Accepted: 7 May 2026
Published: 10 May 2026

Copyright: © 2026 by the authors. Licensee MDPI, Basel, Switzerland. This article is an open access article distributed under the terms and conditions of the Creative Commons Attribution (CC BY) license.

of online simulations. This capability is particularly valuable for digital twin applications in hydraulic turbines operating under rapidly varying renewable energy conditions.

Keywords: Francis turbine; draft tube; sparse sensors; vortex rope; POD; LSTM

1. Introduction

With the acceleration of global energy transition, the share of renewable energy sources—represented by solar photovoltaics, wind power, and biomass energy—in power systems has been continuously increasing. However, these energy sources exhibit significant intermittency and volatility, posing severe challenges to the secure and stable operation of electrical grids [1]. Hydropower turbines, including pumped-storage units, possess superior characteristics such as rapid response, flexible regulation, and adjustable capacity. These attributes enable them to effectively mitigate the output fluctuations of renewable energy sources, thereby serving as a critical cornerstone for the safe and stable operation of power grids. However, to cope with the drastic fluctuations of renewable energy, turbine units are required to operate frequently and rapidly under varying conditions. This operational regime inevitably induces pronounced unsteady flow phenomena within the flow-passage components, including flow separation, coherent vortices (e.g., vortex rope), and intense pressure pulsations. These phenomena are characterized by strong three-dimensionality, non-periodic temporal behavior, and mutual interactions across different scales. These flow instabilities not only significantly degrade unit efficiency but also serve as the primary triggers for hydraulic vibrations, structural fatigue, and even equipment damage. Consequently, ensuring internal flow stability during wide-range, variable-load regulation processes is a core prerequisite for realizing the regulation potential of hydraulic turbines while guaranteeing their operational safety [2,3].

Traditionally, the understanding of such unsteady flows in hydraulic turbines has relied heavily on Computational Fluid Dynamics (CFD) numerical simulations. The majority of research endeavors have primarily focused on the performance prediction of hydraulic machinery, encompassing critical aspects such as pressure pulsations [4–7], rotor-stator interactions (RSI) [8–10], the characteristic S-shaped instability regions [11–13], and the fluid transient phenomenon [14,15]. While CFD provides high-resolution flow field data, its high-fidelity comes at the expense of computational efficiency. For digital twin applications, which demand real-time synchronization between the physical entity and its virtual counterpart, the exorbitant cost of CFD makes it impractical. This critical gap between the need for real-time performance and the reality of slow simulation speeds necessitates the exploration of efficient surrogate models or data-driven approaches to enable timely condition assessment. In response to the computational limitations of CFD, the field has witnessed a surge in the development of surrogate models for hydraulic turbine. Notably, machine learning algorithms have been widely adopted for tasks ranging from fault diagnosis to performance mapping in hydraulic turbines, owing to their ability to learn nonlinear relationships from operational data [16–18]. However, purely data-driven models may lack the physical interpretability required for dynamic flow field reconstruction. Consequently, an alternative line of research has focused on Proper Orthogonal Decomposition (POD), which extracts dominant coherent structures from flow data to construct a low-dimensional, physics-informed basis [19–21]. While such reduced-order representations are powerful for simulation, translating them into actionable engineering tools requires bridging the gap between simulation data and physical measurements. Recently, several non-intrusive reduced-order modeling approaches combining POD with

neural networks have been proposed to address the trade-off between accuracy and efficiency [22,23]. Wang et al. [22] developed a POD-feedforward neural network framework for unsteady combustion flows, demonstrating that neural networks can effectively approximate the mapping from time/parameter values to POD coefficients. Chen et al. [23] further advanced this paradigm by introducing physics-informed neural networks (PINNs) and physics-reinforced neural networks (PRNNs) that incorporate residual losses of reduced-order equations into training, achieving higher accuracy than purely data-driven models for complex nonlinear problems. However, these methods typically require time and physical parameters as inputs, making them difficult to deploy in real engineering scenarios where only sparse sensor measurements are available. Conversely, in engineering practice, monitoring via a sparse array of pressure sensors installed at critical locations offers the most direct approach; however, this yields extremely sparse local information, failing to capture the holistic structure of the flow. Therefore, a critical scientific challenge lies in fusing the high-fidelity knowledge from CFD models with easily accessible sparse sensor signals to achieve online, accurate reconstruction and prediction of the transient flow field within key turbine components.

To this end, this paper proposes a flow field reconstruction and prediction framework: POD-LSTM networks. The core methodology proceeds as follows: First, a high-fidelity flow field database covering target operating conditions is constructed via CFD simulations. Second, the POD method is employed to extract low-dimensional modal bases characterizing dominant flow structures and their corresponding temporal coefficients from the CFD data, thereby achieving a compact representation of the high-dimensional flow field. Subsequently, an LSTM neural network is constructed to establish a non-linear temporal mapping model between pressure signals from sparsely distributed virtual sensors and the POD temporal coefficients. Finally, the trained model enables the dynamic prediction of POD temporal coefficients based solely on limited real-time monitoring data, which, when combined with the POD modal bases, facilitates the real-time reconstruction of the transient full flow field. To validate the effectiveness and accuracy of this approach, the draft tube of a hydraulic turbine—a component characterized by strongly unsteady, three-dimensional flows and a significant impact on unit stability—is selected as the specific object of study. This research aims to provide a new paradigm combining "physics-model-driven" and "data-driven" approaches for the online monitoring and intelligent diagnosis of internal flow states in hydraulic turbines and other turbomachinery.

2. Methodology

In this section, we will describe in detail the proposed flow field prediction framework, which mainly consists of two core modules: a dimensionality reduction and reconstruction model (POD) and a sparse prediction model based on LSTM. For a systematic study of the energy distribution characteristics and the pressure-velocity coupling mechanism, POD analyses were carried out on the flow field, encompassing different operating conditions, POD methods, and variable combinations.

2.1. Model and Grid

This study focuses on the Francis-99 high-head Francis turbine, a widely recognized benchmark in the hydro-power community [24,25]. The selection of this specific turbine is driven by three critical factors that make it ideal for developing and validating POD-LSTM flow prediction frameworks. First, the Francis-99 project provides an extensive repository of high-fidelity data, including detailed geometry, precise operating conditions, and synchronized experimental measurements (LDV, PIV, and pressure sensors). Second, the turbine has been the subject of numerous rigorous experimental campaigns and high-resolution Compu-

tational Fluid Dynamics (CFD) studies (e.g., RANS, LES, and DES). This wealth of existing literature offers a robust ground truth for validating reduced-order models. Lastly, the highly unsteady flow phenomena within the Francis-99 runner and draft tube—such as vortex rope precession and rotor-stator interactions—present a challenging yet representative testbed for reconstructing global flow fields from sparse sensor data. The availability of both dense CFD fields and discrete sensor locations allows for a realistic simulation of practical monitoring scenarios where only limited measurement points are available.

As shown in Figure 1, the computational domain was divided into six distinct flow sections. The geometric parameters of the Francis-99 turbine model are detailed in Table 1. The turbine features 15 + 15 runner splitter blades, 14 guide vanes, and 28 stay vanes, with a runner inlet diameter of 349 mm.

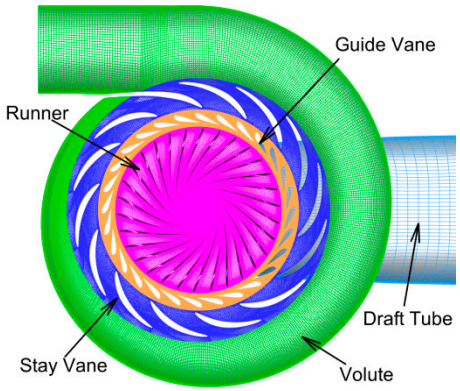


Figure 1. Computational domain of the Francis-99 turbine.

Table 1. Parameters of the Francis-99 turbine.

Parameters	Symbol	Value
Runner blade number	Z_r	15 + 15
Guide vane number	Z_g	28
Stay vane number	Z_s	14
Runner inlet diameter	D_1	349 mm
Runner outlet diameter	D_2	630 mm
Guide vane height	b_0	60 mm

To evaluate the proposed POD-LSTM framework under varying flow regimes, three representative operating points were selected: Part Load (PL), Best Efficiency Point (BEP), and High Load (HL). These conditions were chosen to represent distinct hydraulic behaviors: PL represents off-design operation with swirling vortex ropes; BEP denotes optimal efficiency with stable flow; and HL indicates overload conditions with increased flow instabilities. Critically, these operating points are fully consistent with the experimental test cases established in the Francis-99 Workshop 2, ensuring the validity of the simulation setup and allowing for rigorous benchmarking against established experimental data. The operating parameters for these conditions are summarized in Table 2.

Table 2. Operating Parameters of the Francis-99 turbine.

Parameters	PL	BEP	HL
Guide vane angle (°)	6.72	9.84	12.43
Net head (m)	11.87	11.94	11.88
Discharge (m^3/s)	0.14	0.20	0.24
Runner angular speed (rpm)	332.84	332.59	332.59

The locations of the pressure monitoring points coincide with those of the Francis-99 test rig, and their specific coordinates and descriptions are summarized in Table 3 and Figure 2. This placement was not arbitrary but followed two main rationales. First, to capture the rotational characteristics of the vortex rope, two pairs of symmetric sensors (DT5/DT6 and DT21/DT11) are all installed at the same axial elevation (z = −305.8 mm) but at different tangential positions: DT5 and DT6 are opposite each other, while DT21 and DT11 form another symmetric pair at the same elevation; these multiple symmetric arrangements allow researchers to cross-validate the phase differences between pressure signals generated by the rotating vortex rope, thereby more reliably determining its rotation direction, passing frequency, and propagation behavior around the draft tube circumference. Second, the selected measurement plane lies within the conical part of the draft tube, precisely where the rotating vortex rope (RVR) develops and drives the strongest pressure fluctuations under Part Load (PL) conditions, ensuring that the most significant unsteady pressure phenomena are captured for hydraulic stability analysis.

Table 3. Locations of pressure measuring sensors.

Sensor ID	X (m)	Y (m)	Z (m)
DT5	−0.1491	−0.1006	−0.3058
DT6	0.1491	−0.1006	−0.3058
DT21	0.0904	−0.1566	−0.3058
DT11	−0.0904	0.1566	−0.3058

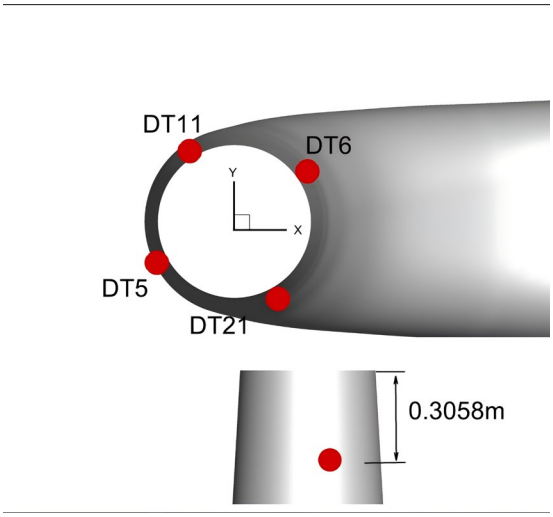


Figure 2. Locations of the sensors (Red dots mean sensor installation positions).

Structured grids generated via ANSYS ICEM 24.0 were used for domain discretization (Figure 3). The boundary layer mesh was refined to achieve an average $y^+ < 35$, with particular focus on the wall surfaces. Numerical simulations were performed using ANSYS Fluent 24.0, imposing total pressure at the inlet, static pressure at the outlet, and no-slip conditions on all walls. Transient effects were captured using the sliding mesh method, initialized from steady-state solutions. The unsteady computation spanned 12 full revolutions with a time step of 2.5×10^{-4} s (equivalent to 0.5° rotation), utilizing the Large Eddy Simulation (LES) turbulence model.

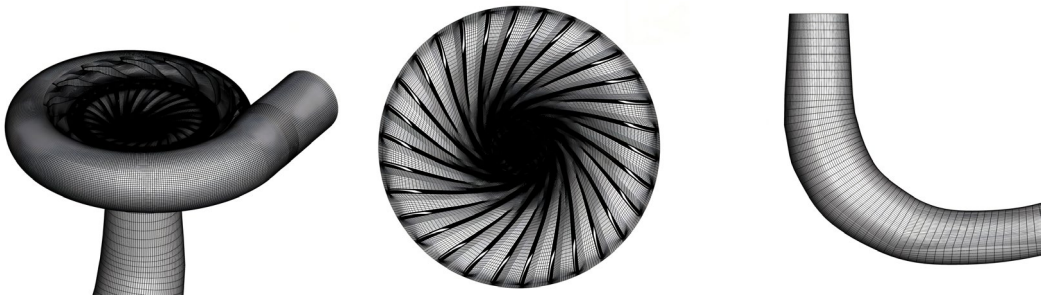
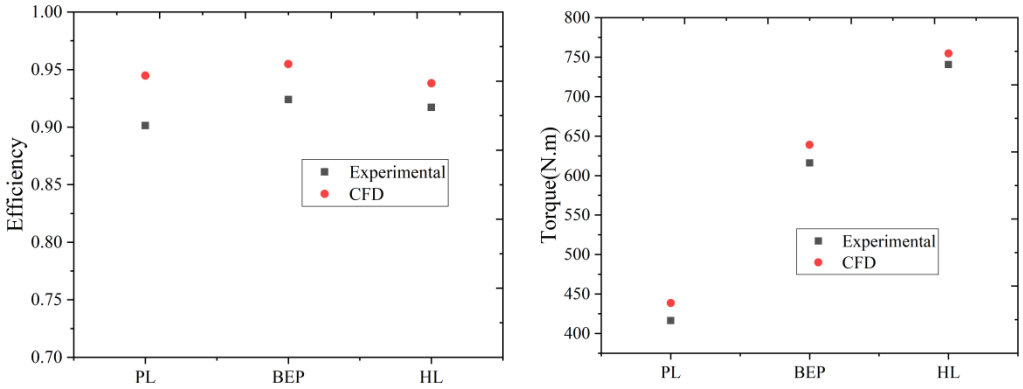


Figure 3. Grid of the Francis-99 turbine.

To validate the accuracy of the numerical computations, a comparative analysis was conducted between the experimental results and CFD predictions regarding efficiency and torque. To account for the pulsations in external characteristic parameters caused by the periodic relative motion between rotating blades and stationary components (e.g., volute, tongue), time-averaged values were utilized for comparison to ensure statistical representativeness and eliminate position-dependent bias. Figure 4 presents the comparison of efficiency and torque under the three operating conditions. The results show that in the PL condition, the CFD-predicted efficiency is 94.48% (experimental: 90.13%) and the torque is 438.58 (experimental: 416.39); in the BEP condition, the CFD-predicted efficiency is 95.47% (experimental: 92.39%) and the torque is 638.97 (experimental: 616.13); in the HL condition, the CFD-predicted efficiency is 93.81% (experimental: 91.71%) and the torque is 754.72 (experimental: 740.54). Overall, the CFD predictions for both efficiency and torque are consistently higher than the experimental values. The deviation between the two decreases gradually as the load increases, showing the closest agreement at the HL condition and relatively larger discrepancies.

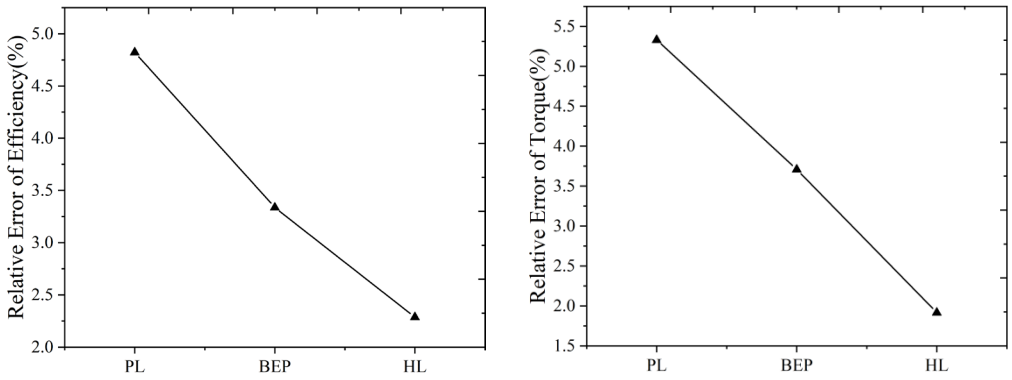


(**a**) Efficiency (**b**) Torque

Figure 4. Comparison of efficiency and torque for different operating conditions.

To clearly illustrate the discrepancies, the relative error distributions for torque and efficiency are further presented in Figure 5. As shown in Figure 5, both the efficiency error and torque error exhibit a monotonic decreasing trend as the operating condition transitions from part-load (PL) to high-load (HL). The minimum errors are observed under the HL condition, with values of 2.29% for efficiency and 1.91% for torque. In contrast, relatively larger errors occur under the PL condition, reaching 4.82% for efficiency and 5.33% for torque. Overall, the relative errors for both torque and efficiency remain within 6%, and under both the best efficiency point (BEP) and HL conditions, the errors are below 4%. These findings validate the fidelity of the present CFD model in predicting external

performance characteristics and confirm satisfactory agreement between the numerical predictions and experimental measurements.



(**a**) Efficiency (**b**) Torque

Figure 5. Relative error of efficiency and torque for different operating conditions.

2.2. POD Method

To extract the dominant coherent structures in the unsteady flow field of a Francis turbine while overcoming the curse of dimensionality and high computational costs associated with high-dimensional flow field data (e.g., CFD grid data or PIV experimental data), this study adopts the Proper Orthogonal Decomposition (POD) technique. POD identifies an optimal set of orthogonal basis functions that minimizes the mean square error in reconstructing the flow field using a limited number of modes, thus maximizing energy capture efficiency [26]. This enables the extraction of low-dimensional coherent structures containing the primary energy from high-dimensional data, achieving effective dimensionality reduction.

2.2.1. Construction of the Snapshot Matrix

Assume we have obtained m snapshots of the flow field of draft tube from numerical simulations at different time steps. Each snapshot contains multiple fundamental physical quantities (such as velocity components u, v, w and pressure p, etc.). To eliminate the influence of dimensional differences among different physical quantities, each physical variable should be nondimensionalized before constructing the snapshot matrix. The specific formulas are as follows:

$$\begin{aligned} p^* &= \frac{p}{0.5\rho_{ref}u_{ref}^2} \\ u^* &= \frac{u}{u_{ref}} \\ v^* &= \frac{v}{u_{ref}} \\ w^* &= \frac{w}{u_{ref}} \end{aligned} \tag{1}$$

where u_{ref} is the average flow velocity at the draft tube inlet section, and $\rho_{ref} = 999.8\ \mathrm{kg/m^3}$ is the density of water.

After that the physical quantities can be reshaped into a column vector of length k (number of cells n multiplied by the number of physical quantities). Assuming the snapshot matrix is constructed from the pressure field p^* and the velocity field u^*, the m snapshots can be arranged in the following form:

$$X = [x_1\ x_2\ \cdots\ x_m] = \begin{bmatrix} p^*(\mathbf{x}_1,t_1) & p^*(\mathbf{x}_1,t_2) & \cdots & p^*(\mathbf{x}_1,t_m) \\ p^*(\mathbf{x}_2,t_1) & p^*(\mathbf{x}_2,t_2) & \cdots & p^*(\mathbf{x}_2,t_m) \\ \vdots & \vdots & \vdots & \vdots \\ p^*(\mathbf{x}_n,t_1) & p^*(\mathbf{x}_n,t_2) & \cdots & p^*(\mathbf{x}_n,t_m) \\ u^*(\mathbf{x}_1,t_1) & u^*(\mathbf{x}_1,t_2) & \cdots & u^*(\mathbf{x}_1,t_m) \\ u^*(\mathbf{x}_2,t_1) & u^*(\mathbf{x}_2,t_2) & \cdots & u^*(\mathbf{x}_2,t_m) \\ \vdots & \vdots & \vdots & \vdots \\ u^*(\mathbf{x}_n,t_1) & u^*(\mathbf{x}_n,t_2) & \cdots & u^*(\mathbf{x}_n,t_m) \end{bmatrix} \quad (2)$$

To focus on the unsteady coherent structures that dominate the turbulent kinetic energy contribution, the mean flow field is subtracted from each snapshot to separate the turbulent fluctuations, thereby constructing the fluctuating snapshot matrix.

$$X' = X - \overline{X}, \quad \overline{X} = \frac{1}{m}\sum_{k=1}^{m} X(:,k) \quad (3)$$

To account for the non-uniformity of the computational mesh in the draft tube, cell volume weights are introduced as $w_i = V_i / V_{ref}$, where V_{ref} is the reference volume (e.g., the average cell volume). The weighted snapshot matrix is constructed as:

$$X' = W^{1/2}X', \quad W = \mathrm{diag}(w_1, w_2, \ldots, w_{2n}) \quad (4)$$

2.2.2. Eigen Decomposition and Mode Extraction

With the fluctuating snapshot matrix constructed, the dominant coherent structures within the flow field can now be extracted by solving the eigenvalue problem of the covariance matrix. This step projects the flow field onto a set of orthogonal bases arranged in descending order of energy, revealing the primary modes that govern the flow fluctuations.

For standard POD, the covariance matrix is defined as $C = \frac{1}{m-1}X'^T X'$. Solving the eigenvalue problem $C\psi_i = \lambda_i \psi_i$ yields the eigenvalues λ_i and eigenvectors ψ_i. The spatial modes are reconstructed as $\phi_i = \frac{1}{\sqrt{\lambda_i(m-1)}}X'\psi_i$, with the temporal coefficients given by $a_i(t_k) = \sqrt{\lambda_i(m-1)}\psi_{ik}$.

For weighted POD, the covariance matrix is defined as $C = \frac{1}{m-1}X'^T W X'$. Solving this eigenvalue problem provides the weighted spatial modes $\phi_i^w = \frac{1}{\sqrt{\lambda_i^w(m-1)}}X'\psi_i^w$ and their temporal coefficients $a_i^w(t_k) = \sqrt{\lambda_i^w(m-1)}\psi_{ik}^w$. These modes satisfy the weighted orthogonality condition $(\phi_j^w)^T W \phi_k^w = \delta_{jk}$ ensuring their independence in the physical space.

2.2.3. Reconstruction of Flow Field

Once the spatial modes and temporal coefficients are obtained, the flow field can be reconstructed at any time instant. According to the fundamental principle of POD, the original fluctuating flow field can be expressed as a linear combination of the modes:

$$X'(:,t_k) = \sum_{i=1}^{r} a_i(t_k)\phi_i \quad (5)$$

where r is the number of modes used for reconstruction. When $r = m$, the original fluctuating flow field is exactly recovered; when $r < m$, a reduced-order approximation is achieved.

2.3. LSTM Method

POD projects high-dimensional flow field data onto a low-dimensional modal space, effectively extracting coherent flow structures. However, as a post-processing method, POD cannot directly predict future flow evolution. To equip POD with predictive capability, time-series modeling of its temporal coefficients is necessary.

Given that the spatial modes are time-independent, the flow dynamics are fully captured by the temporal coefficients. Thus, predicting the future temporal coefficients allows the future flow field to be reconstructed using the existing spatial modes. Based on this idea, this study adopts the LSTM neural network for temporal coefficient prediction. LSTM effectively captures long-term dependencies in time series, making it suitable for modeling the nonlinear evolution of unsteady flows.

Long Short-Term Memory (LSTM) networks were originally proposed by Hochreiter in 1997 [27]. As a specialized variant of Recurrent Neural Networks (RNNs), LSTMs are designed to address the long-term dependency problem encountered by traditional RNNs when processing long sequence data. By introducing a gating mechanism, LSTMs can effectively capture long-term dependencies in sequential data, enabling the network to learn long-range dependencies in sequential data. Each LSTM unit comprises an input gate (i_t), an output gate (o_t), a forget gate (i_t), and a cell state. It receives the hidden state (h_{t-1}) and cell state (C_{t-1}) from the previous time step, along with the current input (x_t), to compute the current hidden state (h_t) and cell state (C_t). The core formulas are as follows:

$$i_t = \sigma\left[W_{ii}x_t + b_{ii} + W_{hi}h_{(t-1)} + b_{hi}\right], \tag{6}$$

$$f_t = \sigma\left[W_{if}x_t + b_{if} + W_{hf}h_{(t-1)} + b_{hf}\right], \tag{7}$$

$$\widetilde{C}_t = \tanh\left[W_{ig}x_t + b_{ig} + W_{hg}h_{(t-1)} + b_{hg}\right], \tag{8}$$

$$o_t = \sigma\left[W_{io}x_t + b_{io} + W_{ho}h_{(t-1)} + b_{ho}\right], \tag{9}$$

$$C_t = f_t c_{(t-1)} + i_t\widetilde{C}_t, \tag{10}$$

$$h_t = o_t\tanh(C_t). \tag{11}$$

2.4. POD-LSTM Framework

As shown in Figure 6, the POD-LSTM framework consists of five steps.

Step 1: Proper Orthogonal Decomposition Analysis. The transient fluctuating data of the three-dimensional draft tube flow field obtained from computational fluid dynamics simulation are constructed into a snapshot matrix X', with dimensions of number of elements (348,400) × number of variables (for example, 2) and a snapshot count of m (180). The proper orthogonal decomposition method is applied to decompose X', yielding the spatial modes and their corresponding temporal coefficients. Dominant modes are retained to characterize the primary dynamical features of the flow field.

Step 2: LSTM Training. In this study, a sliding window approach is employed to construct input-output samples for the long short-term memory (LSTM) network. The input data consist of time series signals acquired from four wall-mounted pressure sensors (designated as DT6, DT5, DT21, and DT11), each containing 3672 time steps of pressure data. The output data are the first two temporal coefficients derived from proper orthogonal decomposition (POD) of the flow field, which characterize the dominant dynamical features of the flow. To establish the mapping relationship between sensor signals and POD coefficients, each POD coefficient serves as an anchor point, and a continuous sequence of 20 time steps of sensor data preceding that anchor point is extracted as an input sample, forming an input tensor of shape (20, 4)

(20 time steps × 4 sensors), with the corresponding output being the two-dimensional POD coefficient vector at the current time point. Based on this sliding window method, a total of 180 input-output pairs are generated and subsequently divided into training and test sets at a ratio of 8:2. The LSTM network architecture consists of a single LSTM layer with a hidden dimension of 64. A dropout layer with a rate of 0.2 is introduced after the LSTM layer to prevent over-fitting, followed by a fully connected layer that maps the hidden state to a two-dimensional output space. The model is trained using mean squared error as the loss function, optimized with the Adam algorithm at an initial learning rate of 0.001, coupled with a learning rate decay strategy to enhance convergence performance. The training process employs a batch size of 8 over 500 epochs, with gradient clipping applied to improve training stability. Through the above approach, the model effectively learns the evolution patterns of flow field modal coefficients from historical sequences of sensor observations, providing a reliable foundation for subsequent flow field reconstruction.

Steps 3–5: Flow Field Reconstruction and Prediction. Using the trained LSTM model, the temporal coefficients for the test samples are predicted. The predicted coefficients are then combined with the spatial modes obtained from POD analysis to reconstruct and predict the flow field, enabling the estimation of the full-field flow state from limited sensor measurements.

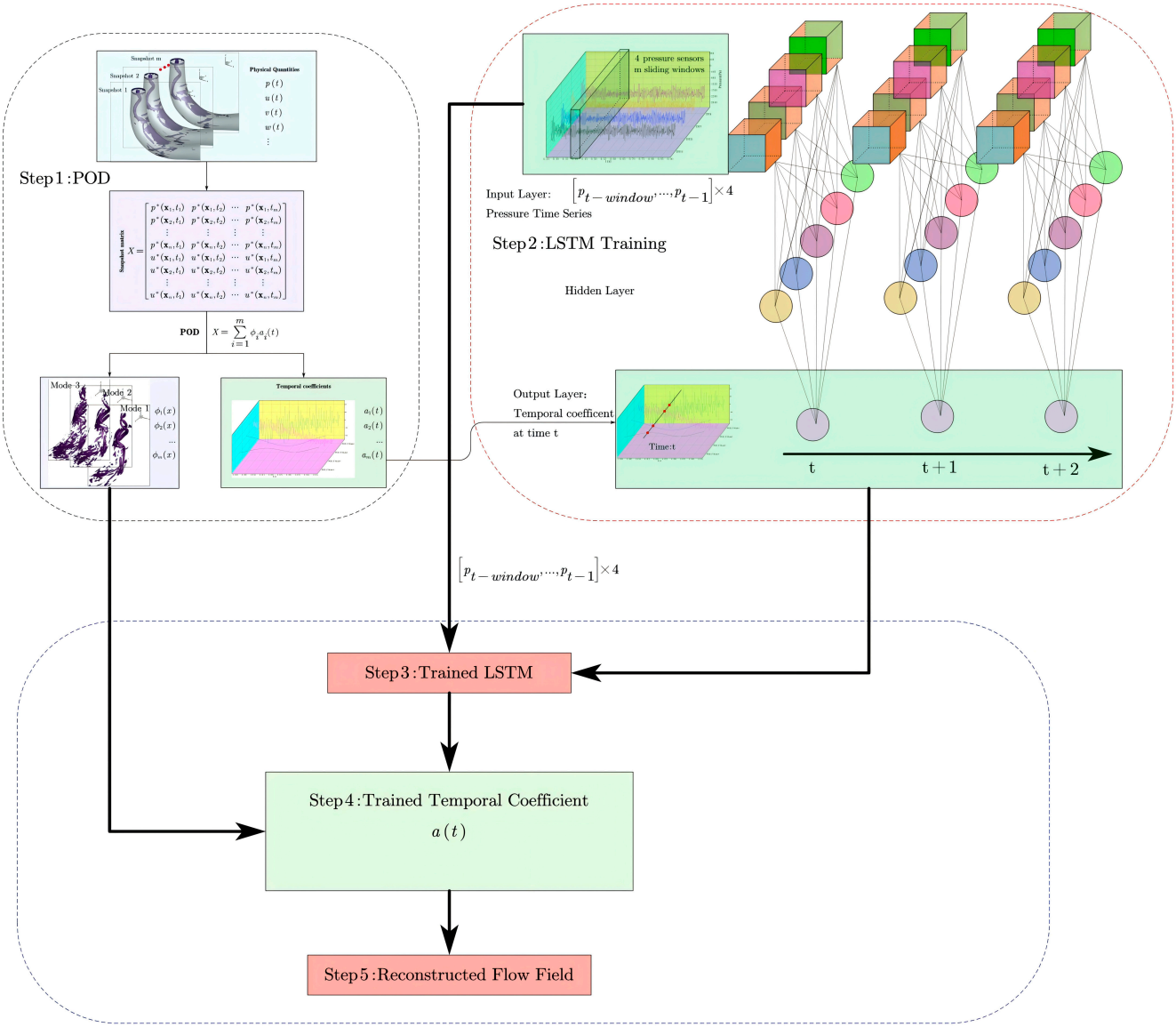


Figure 6. Flowchart of POD-LSTM framework.

3. Result and Discussion

3.1. Standard Snapshots POD and Weighted Snapshots POD

To quantitatively compare the energy convergence under different operating conditions and the contribution of each mode to flow field reconstruction, the energy proportion η_k and the cumulative energy proportion χ_r are introduced as evaluation metrics. The energy proportion of the k-th mode, η_k defines the ratio of its corresponding eigenvalue λ_k to the total energy (the sum of all eigenvalues). The cumulative energy proportion of the first r modes, χ_r, indicates the amount of turbulent kinetic energy captured by the selected dominant modes. They are defined as follows:

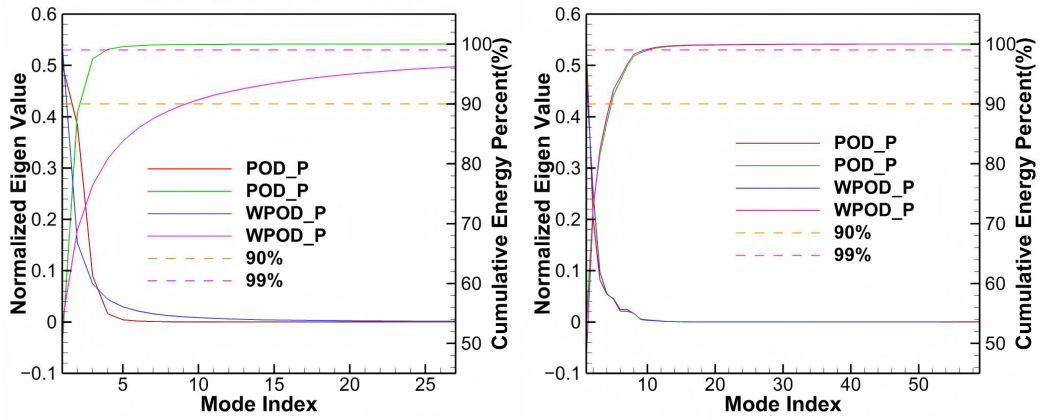
$$\eta_k = \frac{\lambda_k}{\sum_{i=1}^{N} \lambda_i} \tag{12}$$

$$\chi_r = \frac{\sum_{i=1}^{r} \lambda_i}{\sum_{i=1}^{N} \lambda_i} \times 100\% \tag{13}$$

where N is the total number of modes, and r is the number of modes selected.

3.1.1. Mode Energy and Cumulative Mode Energy

Figure 7 presents the pressure field mode energy distribution and cumulative energy percentage obtained via POD and weighted POD under both the PL and HL conditions. As shown in Figure 7a for the PL condition, the first two POD modes of the Standard POD capture 90% of the total energy. In contrast, the weighted POD method exhibits a notably slower energy accumulation, requiring up to the 8th mode to reach the same 90% threshold. Under the HL condition, depicted in Figure 7b, the cumulative energy curves for standard POD and weighted POD almost completely coincide: the first 5 modes capture 90% of the total energy, and the first 11 modes reach 99%. Figure 7 reveals that under the condition with a draft tube vortex rope (PL), the weighting effect is significant, causing notable discrepancies between the two methods. Under the condition without the vortex rope (HL), however, the weighting effect becomes negligible, and the two methods show good agreement.

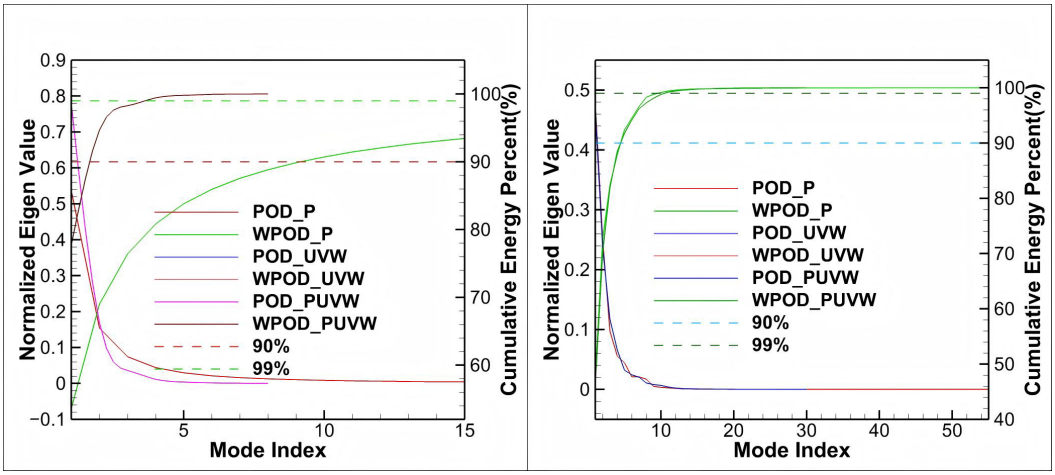


(**a**) Pressure snapshots (PL) (**b**) Pressure snapshots (HL)

Figure 7. Mode energy and cumulative mode energy of POD and weighted POD.

Based on the comparison of the two decomposition methods for the pressure field, we further investigate the modal energy distribution characteristics of weighted POD across

different physical fields—velocity, pressure, and their coupled field—under both PL and HL conditions. Figure 8 compares the energy distribution characteristics of standard POD and weighted POD applied to different physical fields under the PL and HL conditions. Under the PL condition (Figure 8a), the cumulative energy curves for the velocity field (UVW) and the pressure-velocity coupled field (PUVW) almost completely coincide, with the first few modes capturing 90% of the total energy. In contrast, the pure pressure field (P) exhibits a notably slower energy accumulation, requiring significantly more modes to reach the same threshold. Under the HL condition (Figure 8b), the energy variation patterns and eigenvalue distributions for all three physical fields are nearly identical, showing no significant differences. The analysis of Figures 7 and 8 demonstrates that the applicability of weighted POD—and the necessity of employing it over standard POD—depends critically on two factors: the flow condition and the choice of physical variables. Under flow conditions with strong coherent structures such as the vortex rope (PL), the weighting effect is pronounced. In such cases, standard POD may overestimate energy concentration, particularly for the pressure field, where weighted POD exhibits a significantly slower energy accumulation (Figure 7a). Moreover, under the same PL condition, the energy distribution characteristics vary considerably across different physical fields, with the pressure field showing notably slower convergence compared to the velocity and coupled fields (Figure 8a). Under flow conditions without such coherent structures (HL), however, the weighting effect becomes negligible: standard POD and weighted POD yield nearly identical energy distributions (Figure 7b), and the choice of physical variables has little impact on the results (Figure 8b). Therefore, in practical applications, the selection between standard POD and weighted POD should be guided by both the flow regime characteristics (e.g., presence or absence of coherent vortex structures) and the specific physical variables of interest, to avoid misinterpretation of energy distribution characteristics due to inappropriate method selection.



(**a**) PL (**b**) HL

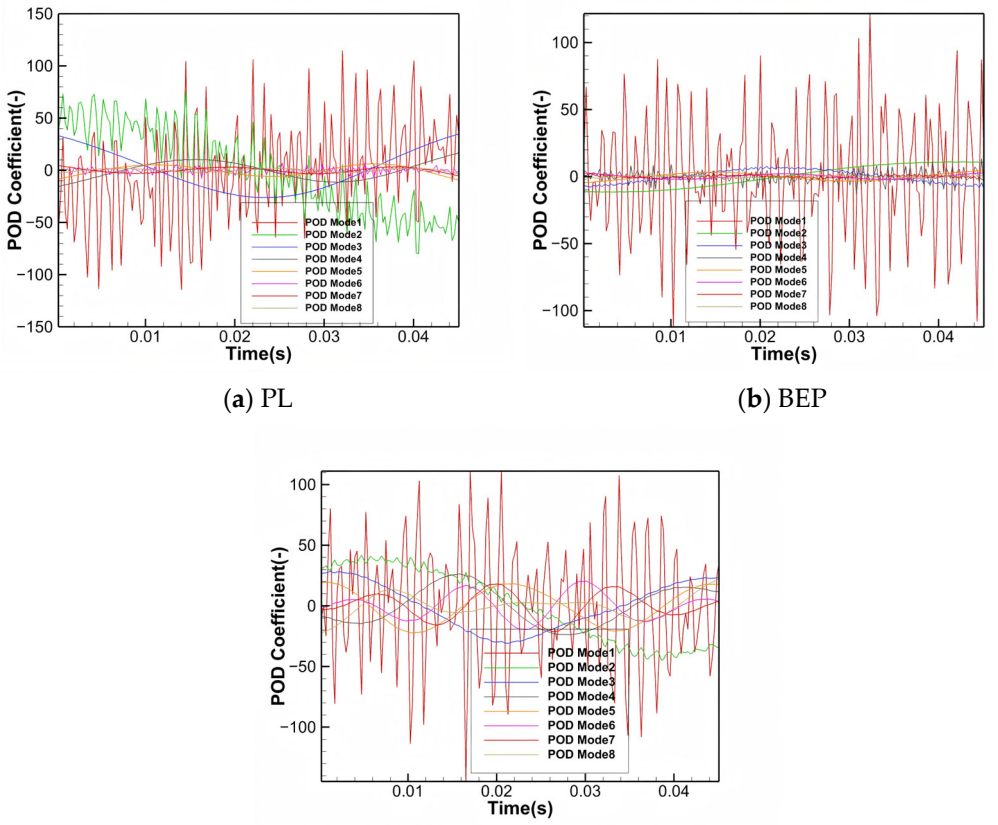
Figure 8. Mode energy and cumulative mode energy for different operating conditions.

3.1.2. Temporal Coefficients

Figure 9 presents the temporal evolution of POD mode coefficients under the PL, BEP, and HL conditions.

Figure 9a shows the temporal evolution of the first eight POD modes under the PL condition. The temporal coefficients of modes 1 and 2 exhibit irregular oscillations around zero with large amplitudes (±100). In contrast, from mode 3 to mode 8, the temporal coefficients display smooth and regular sinusoidal variations, revealing the presence of

weak but orderly periodic flow structures embedded within the vortex-dominated flow regime. Although these structures contribute relatively low energy, they possess well-defined dynamic characteristics.



(**a**) PL (**b**) BEP

(**c**) HL

Figure 9. Temporal evolution of POD coefficients under PL, BEP, and HL conditions.

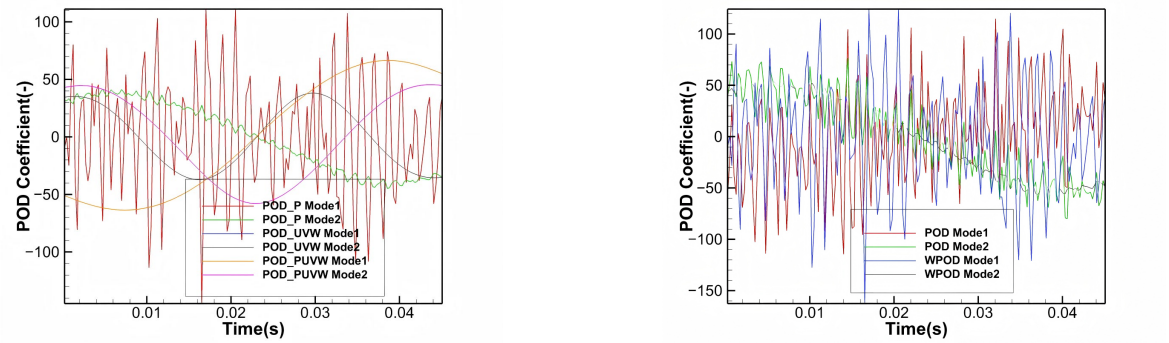
Figure 9b presents the temporal evolution of the first eight POD modes under the BEP condition. Mode 1 exhibits large-amplitude fluctuations. Modes 2 and 3 display predominantly sinusoidal oscillations superimposed with noticeable high-frequency fluctuations. From mode 4 onward, the temporal coefficients become smooth and regularly sinusoidal, indicating that these low-energy modes capture relatively pure periodic coherent structures within the flow field.

Figure 9c presents the temporal evolution of the first eight POD modes under the HL condition. Mode 1 also exhibits large-amplitude irregular fluctuations. Modes 2 and 3 display similar oscillatory patterns to those observed under the BEP condition, but with notably larger amplitudes, indicating enhanced periodic flow structures under the high-load regime. From mode 4 onward, the temporal coefficients become smooth and regularly sinusoidal.

A synthesis of the temporal evolution of POD mode coefficients under the three conditions presented in Figure 9 reveals distinct modal stratification characteristics. Mode 1 exhibits large-amplitude irregular fluctuations across all conditions, displaying a non-periodic temporal behavior. Modes 2 and 3 generally display sinusoidal oscillations, though their regularity varies with the operating condition, with high-frequency fluctuations superimposed in some cases, forming a transitional layer from non-periodic fluctuations to periodic structures. From mode 4 onward, all conditions exhibit smooth and regularly sinusoidal oscillations, indicating that the higher-order modes capture low-energy yet temporally well-defined periodic coherent structures. The primary differences among the three conditions lie in the amplitude and frequency of these higher-order modes: under the

PL and HL conditions, the amplitudes are relatively large (approximately ±30), while under the BEP condition, the amplitudes are notably smaller (approximately ±10), indicating that the periodic structures are stronger under the PL and HL conditions. Regarding frequency, the HL condition exhibits a notably higher oscillation frequency compared to the PL and BEP conditions, reflecting the higher characteristic frequency of flow structures under high-load regimes.

Figure 10 presents the temporal evolution of POD coefficients under different conditions. As shown in Figure 10a, for the standard POD analysis for HL condition, mode 1 of the pressure field exhibits irregular large-amplitude fluctuations, while mode 2 displays predominantly sinusoidal oscillations with noticeable high-frequency fluctuations superimposed. In contrast, the temporal coefficients for both the velocity field (UVW) and the pressure-velocity coupled field (PUVW) display smooth and regular sinusoidal characteristics. Particularly interesting is that mode 1 of the velocity field coincides exactly with mode 2 of the pressure-velocity coupled field. Figure 10b compares the temporal evolution of POD coefficients obtained via standard POD and weighted POD under the PL condition. For mode 1, both methods exhibit large-amplitude irregular fluctuations, but with a noticeable phase difference between them. Mode 2 displays nearly identical oscillatory patterns for both methods, with standard POD showing slightly larger peak amplitudes compared to weighted POD.



(**a**) HL condition: temporal coefficients for different fields (**b**) PL condition: standard POD vs. weighted POD

Figure 10. Temporal evolution of POD coefficients under different conditions: (**a**) comparison across physical fields under HL condition; (**b**) comparison between standard and weighted POD under PL condition.

These observations reveal that the temporal characteristics of POD modes exhibit distinct patterns across different physical fields, providing important guidance for field selection in practical applications. The pressure field exhibits the most pronounced modal stratification: mode 1 captures incoherent background turbulent fluctuations with irregular large-amplitude temporal coefficients, while higher-order modes correspond to periodic coherent structures with regular oscillatory coefficients. This characteristic makes the pressure field particularly suitable for distinguishing coherent structures from background fluctuations in the flow field, offering unique advantages in flow control and fault diagnosis (e.g., draft tube vortex rope detection). In contrast, the velocity field and the pressure-velocity coupled field exhibit smooth and regularly sinusoidal oscillations starting from mode 1, with dominant periodic structures directly captured in low-order modes, making them more suitable for rapid identification of coherent structures and reduced-order flow field modeling. Among these, the pressure-velocity coupled field integrates multi-physics information and exhibits more concentrated energy distribution, enabling high-precision flow field reconstruction with fewer modes.

3.1.3. Spatial Modes and Reconstruction Flow Field

Figure 11 presents the first three spatial modes extracted under the PL condition using both standard POD and weighted POD methods. A comparative analysis reveals that both approaches capture dominant flow structures exhibiting highly consistent physical patterns. Specifically, the first mode clearly reconstructs the typical large-scale double-helical vortex rope structure within the draft tube. As the dominant mode accounting for 50% of the total energy, it characterizes the most intense coherent precessing motion under low-load conditions. In the second mode, while the double helical signature remains discernible, its intensity is significantly attenuated; acting as an orthogonal complement to the first mode, these two collectively form the core framework describing the periodic evolution of the vortex rope. By the third mode, the large-scale helical morphology largely dissipates, fragmenting into scattered small-scale vortices, which visually elucidates the physical process of energy cascading from large-scale coherent structures to small-scale turbulent dissipation. Although both standard POD and weighted POD exhibit high consistency in capturing the macroscopic flow topology, a detailed comparison reveals notable differences in feature extraction precision. Specifically, compared to standard POD, weighted POD resolves the vortex core of the double-helical vortex rope with greater clarity, yielding sharper boundaries and more pronounced low-pressure center characteristics. Additionally, weighted POD effectively suppresses spurious small-scale vortices near the wall regions that are present in the standard POD results, resulting in a cleaner flow field background. These advantages make weighted POD particularly suitable for applications requiring high-fidelity feature extraction from flow fields with strong coherent structures. To further validate the accuracy of the extracted vortex structures, Figure 12 presents Q-criterion contours and streamlines at multiple cross-sections within the draft tube. The streamlines, which represent the actual flow trajectories, clearly delineate the double-helical vortex core. A comparison reveals that the regions identified by the Q-criterion coincide well with the vortex cores indicated by the streamlines, demonstrating that the Q-criterion effectively captures the coherent vortex core with high accuracy and provides a reliable representation of the underlying flow topology.

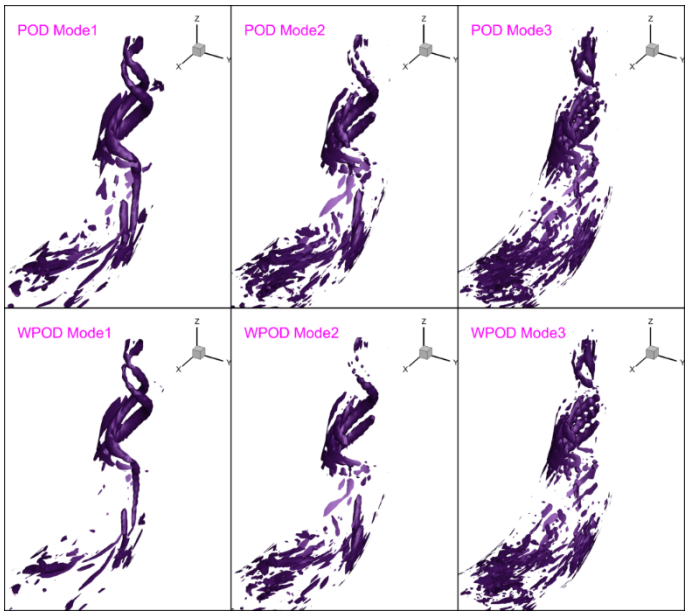


Figure 11. Comparison of the first three spatial modes obtained by Standard POD and Weighted POD under PL conditions (Q-criterion isosurface at Q = 0.005).

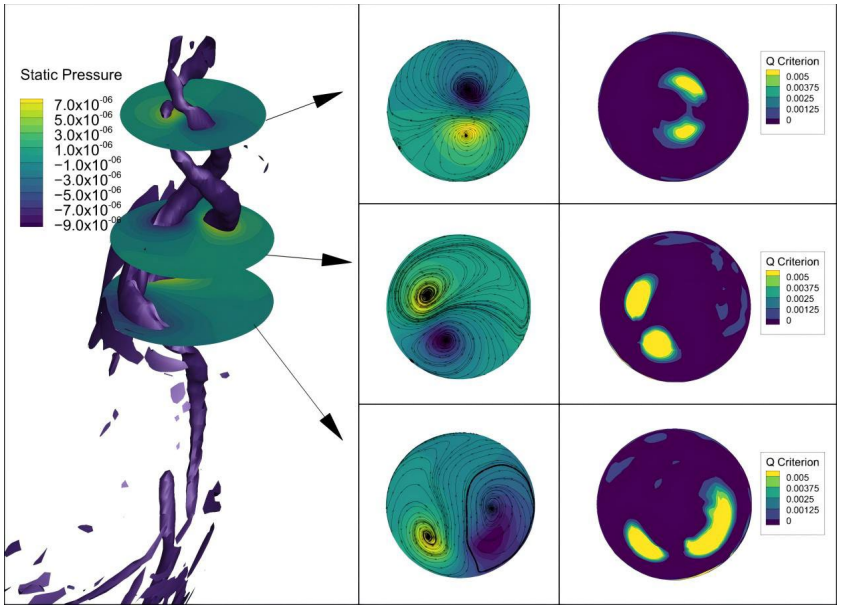


Figure 12. Q-criterion contours and streamlines of draft tube sections under PL conditions.

Figure 13 presents a comparison of the first three spatial modes obtained via Weighted POD and Standard POD under the Best Efficiency Point (BEP) condition. The figures reveal significant changes in the flow structure: large-scale vortical structures in the draft tube cone section have essentially disappeared, indicating a stabilization of the flow, while primary vortex activity is concentrated along the inner side of the draft tube elbow. This distribution reflects a transformation in the vortex rope morphology from a helical shape to a locally wall-attached pattern under BEP conditions. Furthermore, a comparison of the two methods shows that the modes extracted by Weighted POD exhibit fewer vortices near the walls, resulting in a cleaner flow field background.

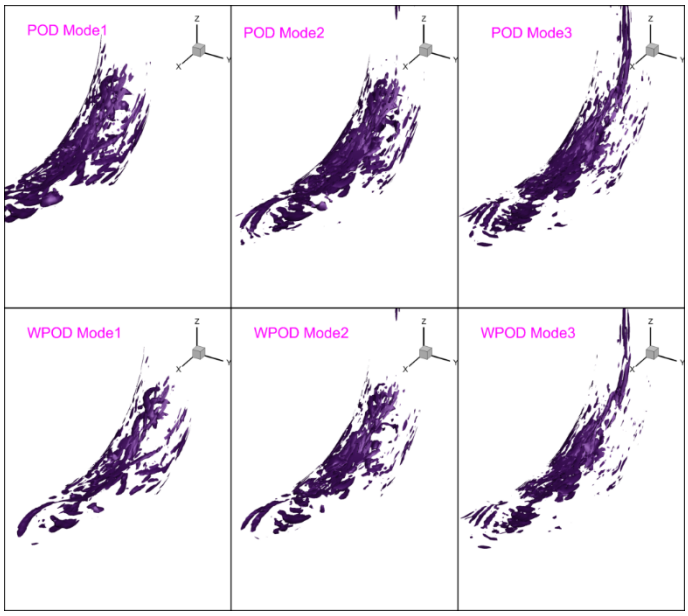


Figure 13. Comparison of the first three spatial modes obtained by Standard POD and Weighted POD under BEP conditions (Q-criterion isosurface at Q = 0.005).

Figure 14 compares the first three modes extracted by weighted POD and standard POD under the high-load (HL) condition. While both methods capture fundamentally consistent evolutionary patterns, weighted POD exhibits notably higher clarity and pre-

cision in the spatial distributions. For mode 1, the vortex structures identified by both methods extend downstream along the draft tube centerline, with intensity gradually increasing and exhibiting a relatively diffuse distribution. As the mode order increases, the vortex structures become increasingly concentrated near the central region of the draft tube. Specifically, weighted POD yields vortex structures that are highly concentrated near the central axis, with well-defined boundaries and minimal spatial smearing, whereas standard POD exhibits more diffuse vortex distributions and noticeable spurious vortex activity near the wall regions.

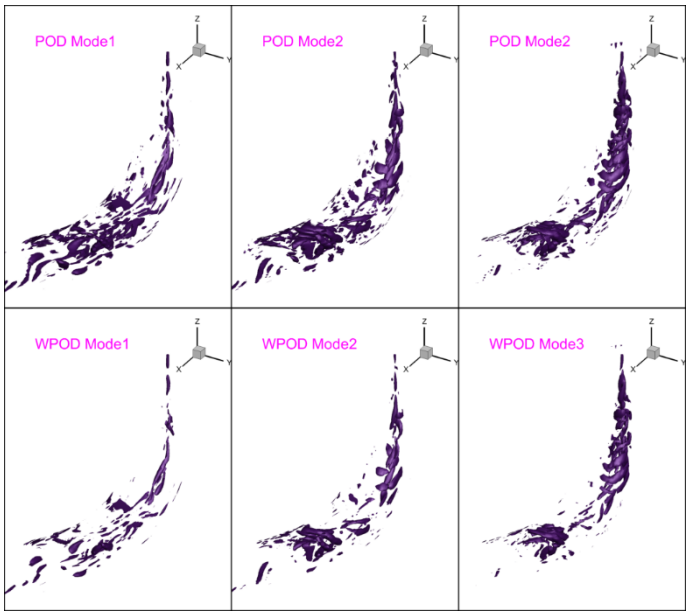


Figure 14. Comparison of the first three spatial modes obtained by Standard POD and Weighted POD under HL conditions (Q-criterion isosurface at Q = 0.005).

Synthesis of the analyses in Figures 11–14 reveals that weighted POD consistently demonstrates superior feature extraction capability across all operating conditions. The comparison shows that weighted POD resolves vortex cores with greater clarity, effectively suppresses spurious small-scale vortices near wall regions, and yields a cleaner flow field background. Meanwhile, the flow structures exhibit distinct characteristics under different conditions: a typical double-helical vortex rope under the PL condition, disappearance of large-scale vortical structures under the BEP condition, and diffuse vortex distribution along the centerline under the HL condition. Overall, while maintaining consistency in capturing the macroscopic flow topology, weighted POD significantly enhances feature extraction precision and physical fidelity, making it particularly suitable for high-fidelity flow field analysis in flow scenarios with strong coherent structures.

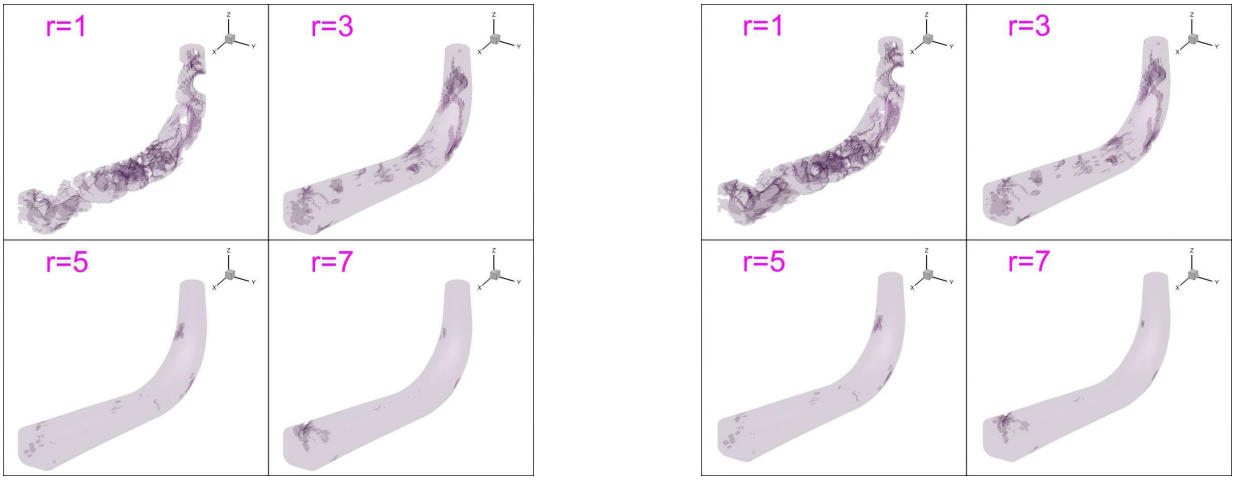
3.1.4. Reconstruction Error of Flow Field

To further quantify the reconstruction fidelity, this section examines the spatial distribution characteristics of the maximum discrepancies between the reconstructed and original flow fields, using the pressure field as a representative case. The relative error is employed to quantify the discrepancy between the reconstructed and original flow fields. For pressure p, the relative error e is defined as the absolute difference between the reconstructed value (p_{rec}) and the original value (p_{ori}), normalized by the magnitude of the original value:

$$e = \frac{|p_{ori} - p_{rec}|}{|p_{ori}|} \tag{14}$$

This metric provides a dimensionless measure of reconstruction accuracy, facilitating comparison across regions with varying magnitudes.

Figure 15 compares the reconstruction error distributions under the PL condition for standard POD and weighted POD. The figure shows that when the relative error exceeds 10%, the spatial distribution characteristics of the reconstruction errors are highly consistent between the two methods.



(**a**) PL condition: Standard POD (**b**) PL condition: Weighted POD

Figure 15. Comparison of reconstruction error distributions: Standard vs. Weighted POD (relative error > 10%).

For the first mode, the high-error region spans the entire draft tube from inlet to outlet, reflecting that a single mode is insufficient to reconstruct the flow field with strong coherent structures. As the mode order increases to the 3rd order, the high-error area converges to the vortex core in the center of the conical section and the outlet region, suggesting that the dominant coherent structures are gradually captured. By the 5th order, the error range shrinks significantly, becoming confined to the inner and outer sides of the elbow section, indicating that the reconstruction captures most of the large-scale flow features. Finally, at the 7th order, the high-error region diminishes further, demonstrating superior reconstruction accuracy with only localized discrepancies remaining.

Notably, despite the similarity in spatial distribution, weighted POD consistently achieves lower error magnitudes at each mode order, reflecting its enhanced fidelity in capturing the essential flow features.

Figure 16 compares the spatial distribution of flow field reconstruction errors across three operating conditions: partial load (PL), best efficiency point (BEP), and high load (HL). At the first mode, significant error regions under both PL and HL conditions span the entire draft tube; however, errors in the HL case are more localized along the central axis. In contrast, the BEP condition exhibits minimal errors in the conical section, with discrepancies confined primarily to the elbow. Upon increasing to the 3rd-order mode, distinct divergence emerges: the high-error zone in the PL case contracts to the vortex core, whereas in the HL case, it becomes diffuse across the upstream and downstream regions of the elbow. For BEP, while errors remain centered in the elbow, their spatial extent is minimized. By the 5th-order mode, large error regions have substantially attenuated in all cases except HL.

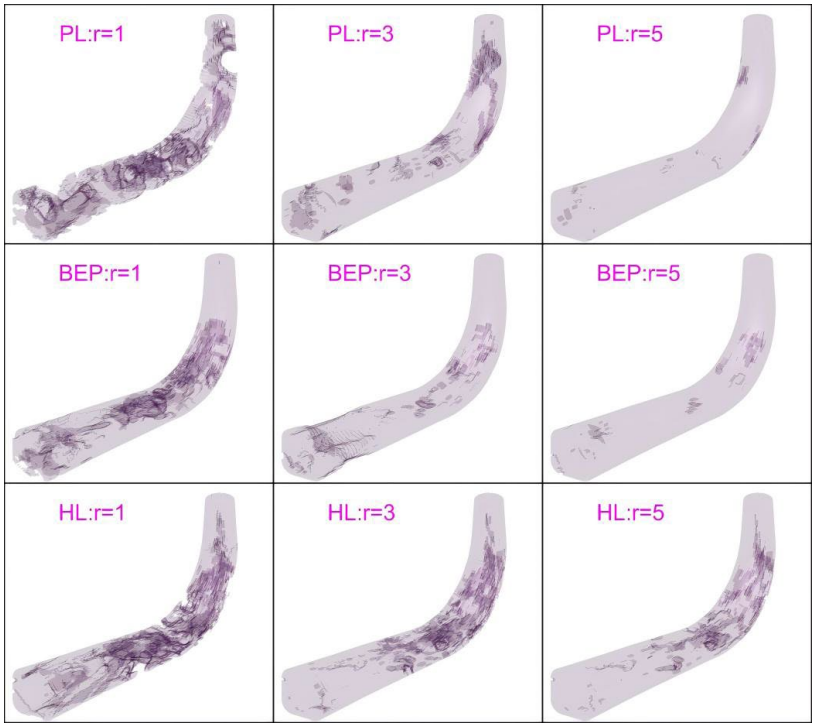


Figure 16. Comparison of reconstruction error distributions under PL, BEP, and HL conditions (relative error > 10%).

3.2. Predictive Performance of the LSTM Network

When constructing the LSTM model to predict POD temporal coefficients, the input data are selected as time-series pressure signals acquired from sparsely arranged pressure sensors on the draft tube wall. It is worth noting that all pressure sensor data used for the LSTM model are obtained from CFD numerical simulations. The choice of prediction target significantly influences the evaluation of model performance. As shown in Figures 9 and 10, the temporal characteristics of POD mode coefficients vary considerably across different physical fields and operating conditions. Among these, the POD temporal coefficients of the velocity field and the pressure-velocity coupled field exhibit smooth and regularly sinusoidal oscillations starting from mode 1, making such periodic signals relatively easy to capture in time-series prediction tasks. In contrast, mode 1 of the pressure field exhibits large-amplitude, non-periodic irregular fluctuations across all operating conditions, posing the greatest challenge for prediction. Therefore, this study selects the pressure field POD temporal coefficients as the prediction target and evaluates the model under three operating conditions—PL, BEP, and HL—to comprehensively assess the predictive capability of the LSTM model across different flow regimes using this most challenging scenario. If the model achieves high-precision predictions for such highly non-periodic and strongly nonlinear signals, its applicability to more regular flow scenarios will be sufficiently validated.

3.2.1. Energy Composition of the Pressure Field

Before evaluating the LSTM prediction performance, it is essential to clarify the energy composition of the pressure field, as this directly determines the practical impact of prediction errors on the final reconstruction.

Table 4 summarizes the energy distribution between the mean flow and the fluctuating field for the three operating conditions. The mean flow accounts for 86.66–98.07% of the total energy and is known a priori, requiring no prediction. The POD analysis and LSTM predictions are applied exclusively to the fluctuating field, which constitutes only

1.93–13.34% of the total energy. From PL to HL, the mean flow energy ratio increases from 86.66% to 98.07% while the fluctuating energy decreases from 13.34% to 1.93%, indicating that the HL condition exhibits considerably more stable flow, with fluctuating energy accounting for less than 2% of the total energy. The total energy of HL (1.91×10^6) is substantially higher than that of PL (2.72×10^5), reflecting the higher mean pressure level under high-load operation.

Table 4. Energy composition of the pressure field for three operating conditions.

Condition	Mean Flow Energy	Fluctuating Energy	Total Energy
PL	86.66%	13.34%	2.72×10^5
BEP	95.98%	4.02%	4.55×10^5
HL	98.07%	1.93%	1.91×10^6

3.2.2. POD Energy Spectrum of the Fluctuating Field

The prediction performance of the LSTM for POD temporal coefficients, as summarized in Table 5, can be physically interpreted through the spatial characteristics of each mode revealed in Figures 11, 13 and 14, considering that the four pressure sensors are mounted on the upper wall of the draft tube cone. For the PL condition (Figure 11), Mode 1 captures the large-scale double-helical vortex rope with strong coherent precessing motion (50.1% of the fluctuating energy), while Mode 2 acts as its orthogonal complement (38.4% of the fluctuating energy). Both modes exhibit spatial structures that extend to the upper cone wall where the sensors are located, maintaining sufficient correlation with the measurements and enabling the LSTM to achieve $R^2 = 0.850$ for Mode 1 and $R^2 = 0.513$ for Mode 2. In contrast, Mode 3 fragments into scattered small-scale vortices (9.0% of the fluctuating energy) that are largely confined away from the wall, exhibiting weak correlation with the sensor locations and leading to a negative R^2 of -3.366. For the BEP condition (Figure 13), large-scale vortical structures in the draft tube cone have essentially disappeared, and the vortex rope has transitioned from a helical shape to a locally wall-attached pattern along the elbow. This flow stabilization results in highly concentrated fluctuating energy in Mode 1 (94.0% of the fluctuating energy), which remains detectable by the wall-mounted sensors and is accurately predicted by the LSTM ($R^2 = 0.96$). Mode 2 contributes only 3.3% of the fluctuating energy—substantially lower than Mode 1's 94.0%—and its spatial structure exhibits weak projection onto the draft tube wall where the sparse sensors are located. Therefore, it is excluded from LSTM prediction, as attempting to predict such a low-energy, poorly observable mode would introduce unnecessary modeling complexity without appreciably improving the reconstructed flow field. Its R^2 value is marked as "—" to indicate that no prediction was performed for this mode. For the HL condition (Figure 14), Mode 1 exhibits vortex structures extending downstream along the draft tube centerline with a relatively diffuse distribution; although diffuse, this large-scale structure still projects onto the upper cone wall, maintaining sufficient sensor correlation for the LSTM to achieve $R^2 = 0.92$. However, Mode 2 displays more diffuse vortex distributions with noticeable spurious vortex activity near the wall regions, but these wall activities are largely uncorrelated with the coherent dynamics of Mode 2, leading to a strongly negative R^2 of -186.6. This indicates that the spatial pattern of Mode 2 is nearly orthogonal to the measurements taken at the upper cone wall. These results collectively demonstrate that the predictability of a POD mode depends not only on its fraction of the fluctuating energy but critically on whether its spatial structure exhibits significant amplitude at the sensor locations. Modes with coherent structures projecting onto the upper cone wall (PL Modes 1–2, BEP Mode 1, HL Mode 1) are reliably predictable, while modes whose energy is concentrated away from the wall or exhibits weak projection at the sensor positions (PL Mode

3, HL Mode 2) cannot be accurately predicted from sparse wall-mounted measurements within the present framework.

Table 5. LSTM prediction performance for POD temporal coefficients.

Condition	Mode	Fluctuating Energy Fraction	R^2
PL	Mode 1	50.10%	0.85
	Mode 2	38.40%	0.513
	Mode 3	9.00%	−3.366
BEP	Mode 1	94.00%	0.96
	Mode 2	3.30%	—
HL	Mode 1	53.10%	0.92
	Mode 2	20.10%	−186.6

Based on these insights, we propose a condition-adaptive strategy that predicts only energetically significant modes with strong spatial correlation to the sensors: PL (Modes 1–2, 88.5% fluctuating energy), BEP (Mode 1, 94.0%), HL (Mode 1, 53.1%). This avoids predicting unobservable modes (e.g., HL Mode 2, PL Mode 3).

3.2.3. Physical Space Reconstruction

It is important to distinguish between two types of R^2 reported in this study. Table 5 presents the prediction accuracy of each individual POD temporal coefficient against its true value, while the R^2 values in Figures 17–19 quantify the temporal consistency of the L_2 reconstruction error—a measure of how stable the reconstruction fidelity remains across test snapshots.

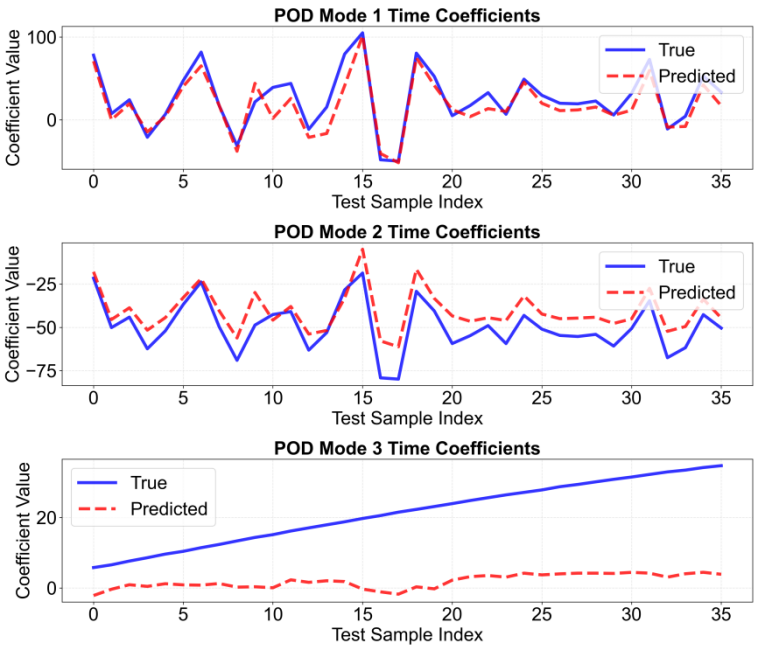


Figure 17. True and predicted temporal coefficients of the first three POD modes under PL condition.

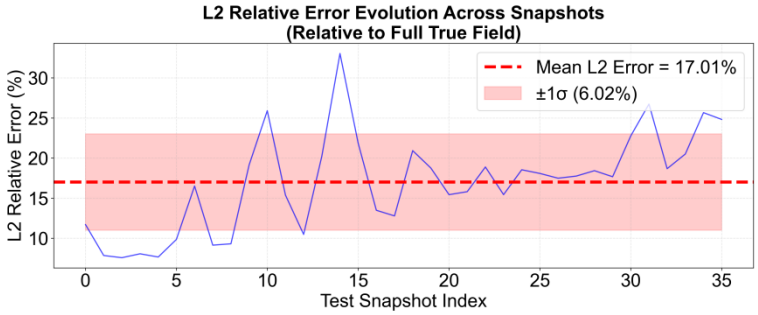


Figure 18. Evolution of the L_2 relative error across 36 test snapshots under the PL condition.

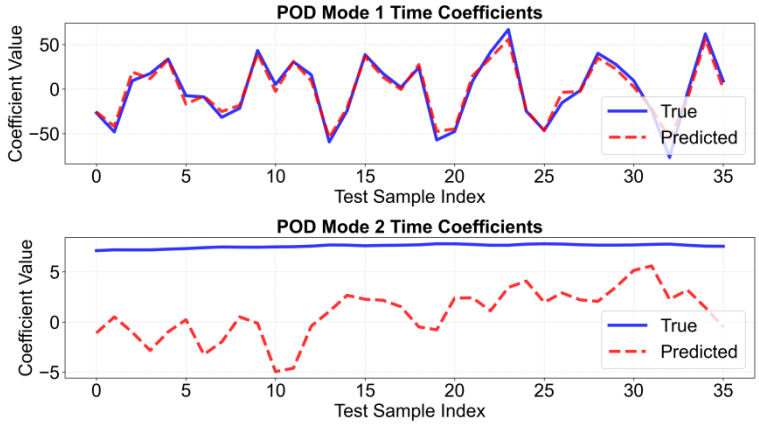


Figure 19. True and predicted temporal coefficients of the first three POD modes under BEP condition.

Figure 17 compares the true and predicted temporal coefficients for the first three POD modes under the PL condition. For Mode 1 and Mode 2, the LSTM model accurately captures the oscillatory trends with nearly synchronized peak and trough positions, indicating no significant phase shift. However, amplitude deviations are evident: Mode 1 exhibits slight alternating overestimation and underestimation, while Mode 2 shows systematic underestimation, particularly at extreme negative fluctuations. In contrast, Mode 3 prediction completely fails to capture the clear linear upward trend of the true coefficients, with predicted values remaining confined to a low-magnitude range, leading to severe amplitude and trend errors. These observations explain the negative R^2 in the coefficient domain, which is dominated by the complete failure of Mode 3 and systematic amplitude underestimation in Mode 2, rather than phase misalignment.

Figure 18 presents the evolution of L_2 relative errors of the reconstructed pressure field across test snapshots under the PL condition, calculated with respect to the full true flow field. The error for each test sample fluctuates around the mean value of 17.01%, with most samples falling within the $\pm 1\sigma$ band of 6.02%, indicating stable overall reconstruction accuracy and a high R^2 of 0.9544.

Figure 19 compares the true and predicted temporal coefficients for the first two POD modes under the BEP condition. For the dominant Mode 1, the predicted coefficients show excellent phase alignment and amplitude agreement with the true values, accurately capturing the primary periodic dynamics of the BEP flow field. In contrast, Mode 2 prediction fails to reproduce the nearly constant true coefficients, instead exhibiting spurious fluctuations with significant deviations. This indicates that the model performs reliably for the high-energy dominant flow structures at BEP, but struggles to resolve the low-energy, near-stationary secondary modes that contribute minimally to the overall flow dynamics.

Figure 20 presents the evolution of L_2 relative errors of the reconstructed pressure field across test snapshots under the BEP condition, calculated with respect to the full true

flow field. The error for each test snapshot fluctuates around the mean value of 7.17%, with most samples falling within the ±1σ band of 2.31%, indicating stable overall reconstruction accuracy and a strong predictive performance.

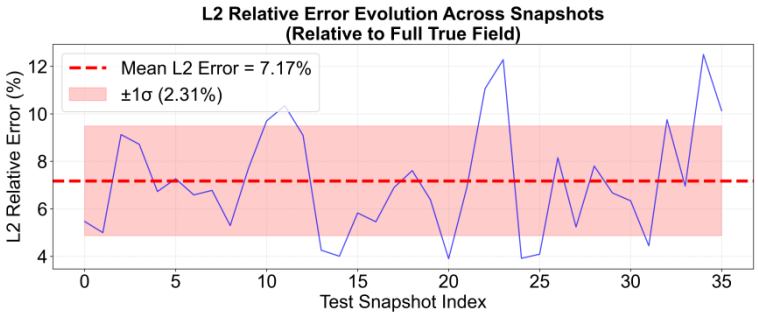


Figure 20. Evolution of the L_2 relative error across 36 test snapshots under the BEP condition.

Figure 21 shows that under the HL condition, the prediction of the POD Mode 1 temporal coefficients is highly accurate, closely matching the true values in both trend and amplitude. However, the prediction for Mode 2 completely fails, with the predicted coefficients showing no correlation to the true signal.

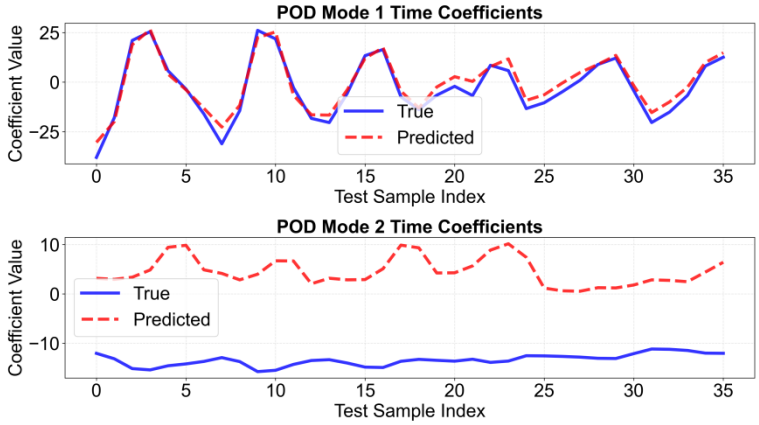


Figure 21. True and predicted temporal coefficients of the first three POD modes under HL condition.

Figure 22 presents the evolution of L_2 relative errors of the reconstructed pressure field across test snapshots under the HL condition, calculated with respect to the full true flow field. The error for each test snapshot fluctuates around the mean value of 12.91%, with most samples falling within the ±1σ band of 1.44%, indicating stable overall reconstruction accuracy and consistent predictive performance despite the complex flow characteristics at high load.

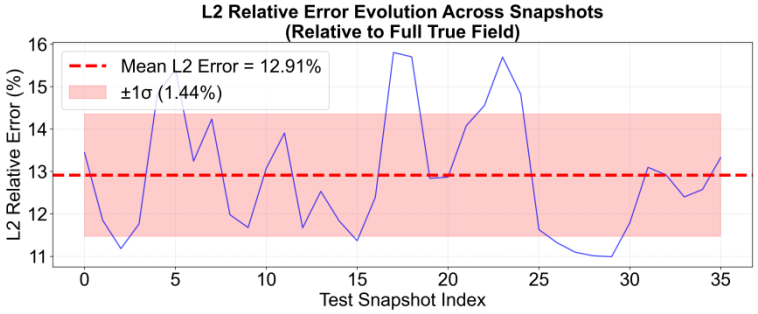


Figure 22. Evolution of the L_2 relative error across 36 test snapshots under the HL condition.

4. Conclusions

This study proposed and validated a POD-LSTM hybrid framework for reconstructing and predicting three-dimensional transient flow fields in the draft tube of a Francis turbine using only four sparse wall-mounted pressure sensors. The key findings are summarized as follows:

(1) The applicability of POD methods depends on both operating condition and the choice of physical variables. Under the PL condition characterized by a strong double-helical vortex rope, the weighting effect is significant: standard POD captures 90% of the total energy with the first 2 modes, while weighted POD requires up to 8 modes to reach the same threshold, indicating that standard POD may overestimate energy concentration in the presence of strong coherent structures. Under the BEP and HL conditions, the energy distributions of standard POD and weighted POD are nearly identical, indicating that the weighting effect on energy convergence becomes negligible. However, weighted POD still yields cleaner spatial modes with sharper vortex boundaries and fewer spurious wall-region vortices even under these conditions, suggesting its advantage for high-fidelity feature extraction regardless of flow regime. Furthermore, temporal coefficients exhibit distinct characteristics across physical fields: the velocity field and pressure-velocity coupled field display regularly sinusoidal oscillations from mode 1 onward, while the pressure field exhibits pronounced modal stratification. In practical applications, weighted POD is recommended when spatial clarity of coherent structures is prioritized, while standard POD suffices for energy distribution analysis under stable flow conditions.

(2) POD temporal coefficients exhibit distinct modal stratification characteristics, but LSTM prediction performance is governed by the spatial correlation between each mode and the sensor locations rather than by temporal regularity. Under all three conditions, mode 1 displays large-amplitude non-periodic fluctuations; modes 2–3 show sinusoidal oscillations with high-frequency modulation; modes 4 and above exhibit smooth regular oscillations. This three-layer structure reflects the inherent energy cascade in draft tube swirling flows. However, prediction performance does not follow this temporal stratification: PL Mode 3 and HL Mode 2, despite their regular temporal oscillations, yield strongly negative R^2 values (-3.366 and -186.6, respectively) because their spatial structures are concentrated away from the wall-mounted sensors. In contrast, modes that project strongly onto the sensor locations—PL Modes 1–2 (R^2 = 0.85, 0.513), BEP Mode 1 (R^2 = 0.96), and HL Mode 1 (R^2 = 0.92)—are reliably predictable. Therefore, the selection of target modes for LSTM prediction should be based on both energetic significance and spatial correlation with available sensor measurements.

(3) Energy composition analysis reveals the practical impact of reconstruction errors. The mean flow accounts for 86.66–98.07% of total pressure energy and is known a priori, requiring no prediction. The POD-LSTM framework operates exclusively on the fluctuating field, which contributes only 1.93–13.34% of total energy. Adopting a condition-adaptive strategy that predicts only modes that are both energetically significant and observable from sparse measurements, the reconstructed pressure fields achieve mean L_2 relative errors of 17.01% (PL), 7.17% (BEP), and 12.91% (HL) with respect to the full true flow field. Given the small contribution of fluctuating energy to total pressure energy, the effective reconstruction error relative to the absolute pressure field is substantially lower than these reported values, making the framework practically viable for engineering applications.

(4) The proposed framework bridges the gap between high-fidelity CFD and real-time monitoring. By combining physics-based dimensional reduction (POD) with data-

driven time-series prediction (LSTM), the method enables full-field flow state estimation from sparse sensor measurements without the computational expense of online CFD simulations. This capability is particularly valuable for digital twin applications in hydraulic turbines operating under rapidly varying renewable energy conditions, where real-time synchronization between physical entities and virtual models is essential for condition assessment and safe operation.

Future work should extend this framework to predict flow fields under transient operating conditions (e.g., start-up, load rejection, and mode switching) and explore the optimal placement of sparse sensors based on the spatial correlation between sensor locations and dominant POD modes. Additionally, integrating the POD-LSTM framework with physics-informed neural networks could further enhance prediction accuracy by enforcing residual losses of reduced-order governing equations during training.

Author Contributions: Conceptualization, L.Z.; methodology, L.Z.; software, L.Z.; validation, Y.L., M.M. and L.K.; data curation, Z.H. and L.X.; writing—original draft preparation, L.Z.; writing—review and editing, all authors (L.Z., Y.L., M.M., L.K., Z.H., L.X. and B.W.). All authors have read and agreed to the published version of the manuscript.

Funding: This research was supported by the Open Research Fund of Hubei Technology Innovation Center for Smart Hydropower (grant number SDCXZX-JJ-2023-15). The APC was funded by the same fund.

Data Availability Statement: The data that support the funding of the study are available on request from the corresponding author. The data are not publicly available due to privacy or ethical restrictions.

Conflicts of Interest: All authors (Ming Ma, Yongbo Li, Lijun Kong, Lintao Xu, Zhenghai Huan) are employees of China Yangtze Power Co., Ltd., which provided funding for this research. The funder had no role in the conceptualization, methodology, investigation, formal analysis, or decision to publish. The authors contributed to data curation, validation, and review and editing of the manuscript. The authors declare no other conflicts of interest.

Nomenclature

POD	Proper Orthogonal Decomposition
WPOD	Weighted Proper Orthogonal Decomposition
LSTM	Long Short-Term Memory
PL	Part load
BEP	Best Efficiency Point
HL	High load
e	Relative error
X	Snapshot matrix
C	Covariance matrix
W	Weights matrix
ϕ	Spatial modes
$a(t)$	Temporal coefficients
r	Number of modes used for reconstruction
χ_r	Cumulative energy proportion
η_k	The ratio of eigenvalue to the total energy

References

1. Trivedi, C.; Cervantes, M.J.; Gunnar Dahlhaug, O. Numerical Techniques Applied to Hydraulic Turbines: A Perspective Review. *Appl. Mech. Rev.* **2016**, *68*, 010802. [CrossRef]
2. Xiong, Y.; Lai, Z.; Liu, X.; Deng, X.; Pang, J. Internal Flow and Pressure Pulsation Characteristics of a High-Head Francis Turbine Under Wide Load Conditions. *Processes* **2025**, *13*, 2939. [CrossRef]

3. Wang, H.; Pang, J.; Lai, Z.; Gan, L.; Huang, D.; Hua, H.; Yu, Z.; Liu, X. Internal Flow Stability of a Francis Turbine under Wide Load Operating Range. *Phys. Fluids* **2025**, *37*, 023346. [CrossRef]
4. Wu, Y.; Liu, S.; Dou, H.-S.; Wu, S.; Chen, T. Numerical Prediction and Similarity Study of Pressure Fluctuation in a Prototype Kaplan Turbine and the Model Turbine. *Comput. Fluids* **2012**, *56*, 128–142. [CrossRef]
5. Yu, A.; Tang, Q.; Wang, X.; Zhou, D.; Liu, J. Investigation of the Pressure Fluctuation Alleviation in a Hydraulic Turbine by Runner Modification. *Water* **2019**, *11*, 1332. [CrossRef]
6. Li, D.; Yu, L.; Yan, X.; Wang, H.; Shi, Q.; Wei, X. Runner Cone Optimization to Reduce Vortex Rope-Induced Pressure Fluctuations in a Francis Turbine. *Sci. China Technol. Sci.* **2021**, *64*, 1953–1970. [CrossRef]
7. Li, D.; Qin, Y.; Wang, J.; Zhu, Y.; Wang, H.; Wei, X. Optimization of Blade High-Pressure Edge to Reduce Pressure Fluctuations in Pump-Turbine Hump Region. *Renew. Energy* **2022**, *181*, 24–38. [CrossRef]
8. Kc, A.; Thapa, B.; Lee, Y.-H. Transient Numerical Analysis of Rotor–Stator Interaction in a Francis Turbine. *Renew. Energy* **2014**, *65*, 227–235. [CrossRef]
9. Li, Z.; Wang, Z.; Wei, X.; Qin, D. Flow Similarity in the Rotor–Stator Interaction Affected Region in Prototype and Model Francis Pump-Turbines in Generating Mode. *J. Fluids Eng.* **2016**, *138*, 061201. [CrossRef]
10. Yang, H.; He, Q.; Huang, X.; Yang, M.; Bi, H.; Wang, Z. Experimental and Numerical Investigation of Rotor–Stator Interaction in a Large Prototype Pump–Turbine in Turbine Mode. *Energies* **2022**, *15*, 5523. [CrossRef]
11. Yin, J.; Wang, D.; Wei, X.; Wang, L. Hydraulic Improvement to Eliminate S-Shaped Curve in Pump Turbine. *J. Fluids Eng.* **2013**, *135*, 071105. [CrossRef]
12. Zhang, W.; Chen, Z.; Zhu, B.; Zhang, F. Pressure Fluctuation and Flow Instability in S-Shaped Region of a Reversible Pump-Turbine. *Renew. Energy* **2020**, *154*, 826–840. [CrossRef]
13. Hu, J.; Zhao, Z.; He, X.; Zeng, W.; Yang, J.; Yang, J. Design Techniques for Improving Energy Performance and S-Shaped Characteristics of a Pump-Turbine with Splitter Blades. *Renew. Energy* **2023**, *212*, 333–349. [CrossRef]
14. Liu, D.; Zhang, X.; Yang, Z.; Liu, K.; Cheng, Y. Evaluating the Pressure Fluctuations during Load Rejection of Two Pump-Turbines in a Prototype Pumped-Storage System by Using 1D-3D Coupled Simulation. *Renew. Energy* **2021**, *171*, 1276–1289. [CrossRef]
15. Yang, X.; Zhang, Z.; Hang, C.; Ding, K.; Du, Y.; Sun, D.; Yang, C. Transient Simulation and Analysis of Runaway Conditions in Pumped Storage Power Station Turbines Using 1D–3D Coupling. *Fluids* **2025**, *10*, 318. [CrossRef]
16. Masood, Z.; Khan, S.; Qian, L. Machine Learning-Based Surrogate Model for Accelerating Simulation-Driven Optimisation of Hydropower Kaplan Turbine. *Renew. Energy* **2021**, *173*, 827–848. [CrossRef]
17. Zhou, T.; Yu, X.; Chen, S.; Zhang, J.; Xu, H. An Intelligent Identification Method of Draft Tube Vortex Rope Based on Dynamic Feature Extraction and Random Forest: Application to a Prototype Pump-Turbine. *J. Energy Storage* **2024**, *102*, 114227. [CrossRef]
18. Wang, J.; Liu, J.; Lu, Y.; Li, H.; Zhang, X. Machine Learning-Driven High-Fidelity Ensemble Surrogate Modeling of Francis Turbine Unit Based on Data-Model Interactive Simulation. *Eng. Appl. Artif. Intell.* **2024**, *133*, 108385. [CrossRef]
19. Kumar, S.; Cervantes, M.; Gandhi, B.K. Flow Field Analysis of Francis Turbine Draft Tube Using POD at Design and Part Load Operating Conditions. *J. Appl. Fluid Mech.* **2024**, *17*, 770–784. [CrossRef]
20. Liu, G.; Sun, L.; Guo, P.; Li, Y.; Wang, W.; Wang, Z. Coherent Structure Analysis of Double-Helix Vortex Rope in Pump Turbine Operating in Turbine Mode Based on POD and DMD. *J. Energy Storage* **2025**, *128*, 117144. [CrossRef]
21. Li, L.; Wang, Z.; Chen, Y.; Li, C. Research on Rapid Simulation of Reduced-Order Model for Pump-Turbine Flow Field. *J. Phys. Conf. Ser.* **2025**, *3150*, 012005. [CrossRef]
22. Wang, Q.; Hesthaven, J.S.; Ray, D. Non-Intrusive Reduced Order Modeling of Unsteady Flows Using Artificial Neural Networks with Application to a Combustion Problem. *J. Comput. Phys.* **2019**, *384*, 289–307. [CrossRef]
23. Chen, W.; Wang, Q.; Hesthaven, J.S.; Zhang, C. Physics-Informed Machine Learning for Reduced-Order Modeling of Nonlinear Problems. *J. Comput. Phys.* **2021**, *446*, 110666. [CrossRef]
24. Trivedi, C.; Cervantes, M.J.; Gandhi, B.K.; Dahlhaus, O.G. Experimental and Numerical Studies for a High Head Francis Turbine at Several Operating Points. *J. Fluids Eng.* **2013**, *135*, 111102. [CrossRef]
25. Trivedi, C. Francis-99 Workshop 2: Transient Operation 2012. 2026. Available online: https://dataverse.no/dataset.xhtml?persistentId=doi:10.18710/WLBL7M (accessed on 29 March 2026).
26. Borée, J. Extended Proper Orthogonal Decomposition: A Tool to Analyse Correlated Events in Turbulent Flows. *Exp. Fluids* **2003**, *35*, 188–192. [CrossRef]
27. Hochreiter, S.; Schmidhuber, J. Long Short-Term Memory. *Neural Comput.* **1997**, *9*, 1735–1780. [CrossRef]

Disclaimer/Publisher's Note: The statements, opinions and data contained in all publications are solely those of the individual author(s) and contributor(s) and not of MDPI and/or the editor(s). MDPI and/or the editor(s) disclaim responsibility for any injury to people or property resulting from any ideas, methods, instructions or products referred to in the content.